Available online at www.sciencedirect.com
SCIENCE DIRECT®
International Journal of Heat and Mass Transfer 47 (2004) 1953–1964
International Journal of HEAT and MASS TRANSFER
www.elsevier.com/locate/ijhmt

Numerical study of fin-spacing effects in annular-finned tube heat exchangers

Mi Sandar Mon, Ulrich Gross *

Institut für Wärmetechnik und Thermodynamik, Technische Universität Bergakademie Freiberg, Gustav-Zeuner-Str. 7, 09599 Freiberg, Germany

Received 25 April 2003; received in revised form 1 September 2003

Abstract

The effects of fin spacing on four-row annular-finned tube bundles in staggered and in-line arrangements are investigated by the three-dimensional numerical study. Renormalization group theory (RNG) based k–ε turbulence model is allowed to predict the unsteady flow and conjugate heat transfer. According to the flow visualization results, the boundary layer developments and horseshoe vortices between the fins are found to be substantially dependent on the fin spacing to height ratio and Reynolds number. The heat transfer and pressure drop results for various fin spacings are presented. In addition, the numerical results are compared with the existing correlations.

Keywords: Finned-tube bundle; Forced convection; Heat transfer; Pressure drop; Numerical

1. Introduction

Annular-finned tube heat exchangers are commonly used in industry (a typical cross-section is shown in Fig. 1). In designing such heat exchangers, it is necessary to note the interactions between the local heat transfer and flow distribution within the fins in cross flow. The relevant literature about the influence of the fin spacing of annular-finned tube banks is quite limited to the experiments [1–7] and respective data [1–3,6] show that the effect of fin spacing is largely influenced by the boundary layer development.

The existence of the horseshoe vortex system close to the fin-tube junction is obvious in the finned-tube heat transfer studies [1,8–11]. Sung et al. [1] examined the occurrence of the horseshoe vortex system in accordance with fin spacing to height changes ($0 < s/h_f < 0.4$) by utilizing mass transfer data and they found additional secondary and ternary vortices which are much smaller than the primary ones.

Kuntysh et al. [2] studied the effect fin spacing to height ratio for staggered arrangement tube bundles for $Re = 5 \times 10^3$ to 5×10^4 and $s/h_f = 0.3$ to 1. They found the Nusselt number to increase in proportion to $(s/h_f)^{0.7}$, although keeping constant in the range of $s/h_f > 0.53$. However, Stasiulevičius and Skrinska [3], and Briggs and Young [4] observed that Nusselt numbers vary with $(s/h_f)^{0.2}$ and $(s/h_f)^{0.14}$, respectively. Therefore, no uniform effect of s/h_f on the heat transfer coefficient is expected, besides the general enhancement of heat transfer when the fin spacing to height ratio is increased.

Jameson [5] found the heat transfer coefficient to be independent of fin spacing; however, the effect on pressure drop is remarkable. Recently, Watel et al. [6] investigated the influence of flow velocity and fin spacing on forced convective heat transfer from a single annular-finned tube. They found that for a fixed Reynolds number, the reduction in fin spacing leads to a decrease of heat transfer. Antuf'ev and Gusev [7] tested five-row staggered bundles with $0.3 \leqslant s/h_f \leqslant 0.96$ and suggested that a stagnation zone is formed at the root of the fin and at the tube surface in cases of smaller fin spacing. This region is swept by a non turbulent flow, and it is excluded from taking part in active heat transfer. Jacobi and Shah [12] proposed that the air flow exhibits all of

* Corresponding author. Tel.: +49-3731-392684; fax: +49-3731-393655.
E-mail address: gross@iwtt.tu-freiberg.de (U. Gross).

0017-9310/$ - see front matter © 2003 Elsevier Ltd. All rights reserved.
doi:10.1016/j.ijheatmasstransfer.2003.09.034

Nomenclature

A	total heat transfer area (m^2)
A_f	surface area of fin (m^2)
A_t	outside surface area of tube except fins (m^2)
c_p	specific heat ($J\,kg^{-1}\,K^{-1}$)
$C_{1\varepsilon}$, $C_{2\varepsilon}$, C_μ	turbulence model constants
d	tube outside diameter (m)
d_{eq}	equivalent diameter as defined in [25] (m)
d_f	fin diameter (m)
Eu	Euler number, $Eu = \Delta p/\rho u_{max}^2$
Eu_m	Euler number, $Eu_m = \Delta p/\rho u_m^2$
$\dot{H}$	flow rate of enthalpy (W)
h	heat transfer coefficient ($W\,m^{-2}\,K^{-1}$)
h	specific enthalpy ($J\,kg^{-1}$)
h_f	fin height (m)
k	thermal conductivity ($W\,m^{-1}\,K^{-1}$)
k	turbulent kinetic energy ($m^2\,s^{-2}$)
n	number of tube rows in direction of flow
Nu	Nusselt number, $Nu = hd/k_a$
Pr	Prandtl number, $Pr = c_p\mu/k_a$
Δp	pressure drop (Pa)
$\dot{Q}$	heat flow rate (W)
Re	Reynolds number, $Re = u_{max}d/v$
$Re_{d,eq}$	Reynolds number, $Re_{d,eq} = u_m d_{eq}/v$
S	fin spacing (m)
S	the modulus of the mass rate-of-stress tensor
S_f	fin pitch (m)
S_{ij}	mean stress rate
S_l	longitudinal tube pitch (m)
S_t	transverse tube pitch (m)
T	temperature (K)
t_f	fin thickness (m)
u	velocity ($m\,s^{-1}$)

Greek symbols

α_p	inverse Prandtl number
β	angle around the tube, measured from the front stagnation point
ε	turbulent energy dissipation rate ($m^2\,s^{-3}$)
η	fin efficiency
θ	logarithmic mean temperature difference (K)
μ	viscosity ($kg\,m^{-1}\,s^{-1}$)
v	kinematic viscosity ($m^2\,s^{-1}$)
ρ	density ($kg\,m^{-3}$)

Subscripts

a	air
eff	effective
f	fin
in	inlet
m	mean
max	maximum
out	outlet
s	solid
t	tube, turbulent
w	wall

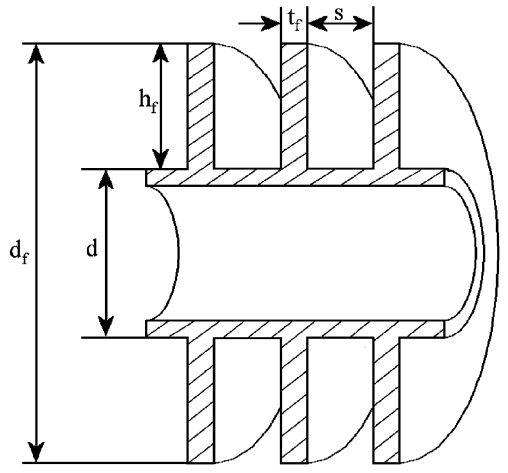

Fig. 1. Cross-section of a typical annular-finned tube.

possible flow features (e.g., steady or unsteady, laminar or turbulent) in a single heat exchanger. They suggested that there were still limitations to the air-side heat transfer performance and a clear understanding of air flow in the complex passages of heat exchangers was needed so that surface designs can be optimised efficiently.

Moreover, it is still difficult and complicated to predict and visualize the flow and related heat transfer features between the geometrically complex bundles by means of experimental investigation [13]. In addition, the heat transfer in a finned-tube heat exchanger is a conjugate problem [14] and it can be established efficiently by the way of numerical means. To provide better understanding of the most important mechanisms of heat transfer in a flow passing through finned-tube heat exchangers, numerical simulations may therefore be a helpful tool.

Previous numerical investigations [9–11,13–18] have been performed for plate-finned tube bundles to evaluate the effect of fin spacing; however, respective calculations are missed for the annular-finned tube heat exchangers. Regardless of the fin spacing effect, only one numerical study for annular-finned tubes was found in Jang et al. [19]. Jang et al. studied numerically and experimentally fluid flow and heat transfer performance in four-row annular-finned tube heat exchangers in staggered arrangement by emphasising the steady and laminar flow conditions.

The purpose of the present study, see also Mon [20], is to investigate the velocity and temperature distributions between the fins of four-row annular-finned tube bundles numerically. It is evident that all past relevant experimental work has been performed for staggered arrangement and in viewing this, numerical investigations are also performed for in-line arrangements. The flow behaviour of the developing boundary layer, the horseshoe vortex system, and thermal boundary layer developments in the annular-finned tube banks will be visualized accordingly.

The secondary aim of the study is also to validate the numerical results. Webb [21] presented an excellent survey for overall heat transfer and pressure drop correlations on annular-finned tube bundles. For staggered tube layout, Webb recommends the heat transfer correlation of Briggs and Young [4] and the pressure drop correlation of Robinson and Briggs [22]. The numerical results are compared with the existing correlations [4,22–25].

2. Numerical simulation

2.1. Computational domains

A schematic view of the proposed in-line and staggered finned-tube bundles are shown in Fig. 2 where the computational domains to be considered in this study are sketched by dotted lines along with the symmetry conditions. The upstream boundary of the computational domain is located at 1.2 times fin diameter from the centre of the first row while the downstream boundary is set as 3.6 times fin diameter from the last row centre line.

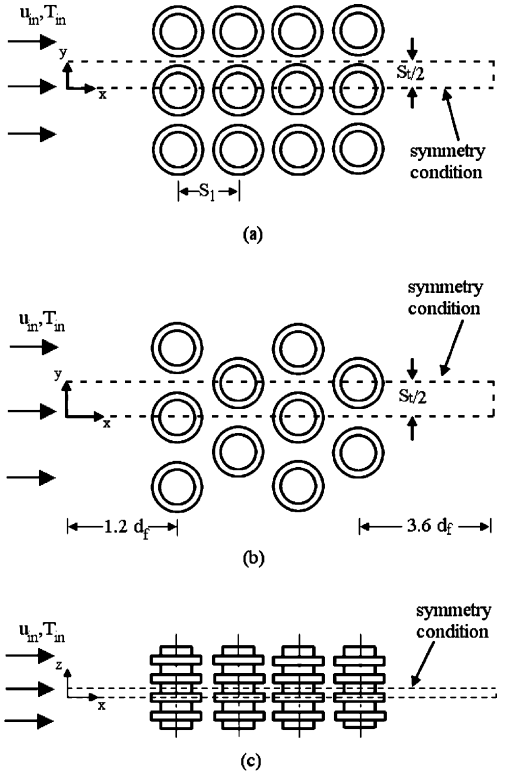

Fig. 2. Computational domains: (a) in-line arrangement, (b) staggered arrangement and (c) top view.

2.2. Governing equations

For consideration of an annular-finned tube heat exchanger under the proposed range of Reynolds numbers, the flow in the finned-tube bundle has been assumed three-dimensional, incompressible, unsteady and turbulent. The Reynolds-averaged equations are,

$$\text{Continuity equation:}\quad \frac{\partial \rho}{\partial t}+\frac{\partial}{\partial x_i}(\rho u_i)=0 \tag{1}$$

Momentum equation:

$$\rho\frac{Du_i}{Dt}=-\frac{\partial p}{\partial x_i}+\frac{\partial}{\partial x_j}\left[\mu\left(\frac{\partial u_i}{\partial x_j}+\frac{\partial u_j}{\partial x_i}-\frac{2}{3}\delta_{ij}\frac{\partial u_l}{\partial x_l}\right)\right]+\frac{\partial}{\partial x_j}\left(-\rho\overline{u_i'u_j'}\right) \tag{2}$$

where

$$-\rho\overline{u_i'u_j'}=\mu_t\left(\frac{\partial u_i}{\partial x_j}+\frac{\partial u_j}{\partial x_i}\right)-\frac{2}{3}\left(\rho k+\mu_t\frac{\partial u_i}{\partial x_i}\right)\delta_{ij} \tag{3}$$

The RNG k–ε model of FLUENT [26] adopts the following transport equations:

$$\rho\frac{Dk}{Dt}=\frac{\partial}{\partial x_i}\left[\alpha_p\mu_{\text{eff}}\frac{\partial k}{\partial x_i}\right]+\mu_t S^2-\rho\varepsilon \tag{4}$$

$$\rho\frac{D\varepsilon}{Dt}=\frac{\partial}{\partial x_i}\left[\alpha_p\mu_{\text{eff}}\frac{\partial \varepsilon}{\partial x_i}\right]+C_{1\in}\frac{\varepsilon}{k}\mu_t S^2-C_{2\in}\rho\frac{\varepsilon^2}{k}-R \tag{5}$$

where effective viscosity $\mu_{\text{eff}}=\mu+\mu_t$, and $\mu_t=\rho C_\mu\frac{k^2}{\varepsilon}$ in the high Reynolds number range with $C_\mu=0.0845$, k as the turbulent kinetic energy, ε as referred to the dissipation rate of k and α_p is the inverse Prandtl number. The rate of strain term R is given by

$$R=\frac{C_\mu\rho\eta^3(1-\eta/\eta_0)}{1+\beta\eta^3}\frac{\varepsilon^2}{k} \tag{6}$$

where $\eta=\frac{Sk}{\varepsilon}$, $\eta_0=4.38$, $\beta=0.012$ and $S^2=2S_{ij}S_{ij}$ is the modulus of the rate of strain tensor expressed as $S_{ij}=\frac{1}{2}(\frac{\partial u_i}{\partial x_j}+\frac{\partial u_j}{\partial x_i})$. The RNG theory gives values of the constant $C_{1\varepsilon}=1.42$ and $C_{2\varepsilon}=1.68$.

$$\text{Energy equation:}\quad \frac{\partial}{\partial t}(\rho E)+\frac{\partial}{\partial x_i}(u_i(\rho E+p))=\frac{\partial}{\partial x_i}\left(k_{\text{eff}}\frac{\partial T}{\partial x_i}\right) \tag{7}$$

where E is the total energy and $k_{\text{eff}}=k+k_t$ the effective conductivity, including the turbulent thermal conductivity k_t.

The following energy transport equation is used within the solid region (fins):

$$\frac{\partial}{\partial t}(\rho c_p T) = \frac{\partial}{\partial x_i}\left(k_s \frac{\partial T}{\partial x_i}\right) \tag{8}$$

The buoyancy and radiation effects have been neglected.

2.3. Boundary conditions

At the upstream boundary conditions, the dry air entering the computational domain is assumed to have uniform velocity u_{in}, temperature T_{in} (308.15 K) and turbulent intensity I (1%) with the velocity components in the y and z directions considered to be zero. The fluid region comprises of the entrance, outlet and bundle zone and the solid region includes the fin. At the solid surfaces, no-slip conditions for the velocity are specified. Heat convection to the fin and heat conduction in the fin are considered. Constant temperature T_w (283.15 K) is assigned to the tube surface and all velocity components are set to be zero. At the symmetry planes, heat flux is assumed zero. The normal velocity component at the symmetry plane is also zero, i.e. no convective flux across that symmetry plane occurs. Thus, the temperature gradients and tangential components of the velocity gradients in normal direction are set equal zero. The flow between the fins is considered as laminar while the other parts of the bundle will be treated as turbulent regions.

2.4. Solution algorithm

In this study, a general curve linear coordinate grid generation system based on body–fitted coordinates is used to discretize the computational domain into a finite number of control volumes. With proper control of the grid density, the computational domain can be considered for two main regions. The finer mesh sizes are prepared near the fin and tube wall to resolve the secondary flows (horseshoe vortices, flow separations) where the high gradients are to be. The coarse mesh sizes are selected for the case where the flow is relatively uniform. The grid generations for staggered and in-line arrangements are shown in Fig. 3. To determine the extent of the grid independence to the results, care is necessarily to be taken for the relative errors in the averaged Nusselt numbers between such grids, which should be less than 5%. Even though there are some limitations on the CPU time and computer resources, 50,000–99,000 cells are used to discretize the computational domains.

Numerical investigations are performed for five and three bundles respectively of the staggered and the in-line tube arrangement, which are summarized in Table 1. All simulations are carried out for a range of Reynolds numbers, $8.6 \times 10^3 \leqslant Re \leqslant 4.3 \times 10^4$ (based on the air velocity through the minimum free flow area and the tube outside diameter). Renormalization group theory (RNG) based k–ε turbulence model is allowed to predict the heat transfer and fluid flow characteristics by using the computational fluid dynamics (CFD) commercial code, FLUENT [26]. The first order upwind numerical scheme and PISO algorithm are utilized to discretize the governing equations.

All the tests are processed with the time increment $\Delta t = 0.001$ s at initial condition and then, it is gradually increased once the calculation proceeds. Numerical simulations were performed with SGI workstation (2 CPU R12000, 300 MHz). One typical calculation with sufficient mesh sizes required about 70–80 h and lengthy calculations are stopped when either a steady or periodic flow was encountered.

3. Data reduction

Enthalpy flow rates of the inlet ($\dot{H}_{in}$) and outlet ($\dot{H}_{out}$) positions of the computational domain are determined by the aid of FLUENT and then the air-side heat transfer rate of the bundle was calculated according to Eq. (9).

$$\dot{Q} = \dot{H}_{out} - \dot{H}_{in} \tag{9}$$

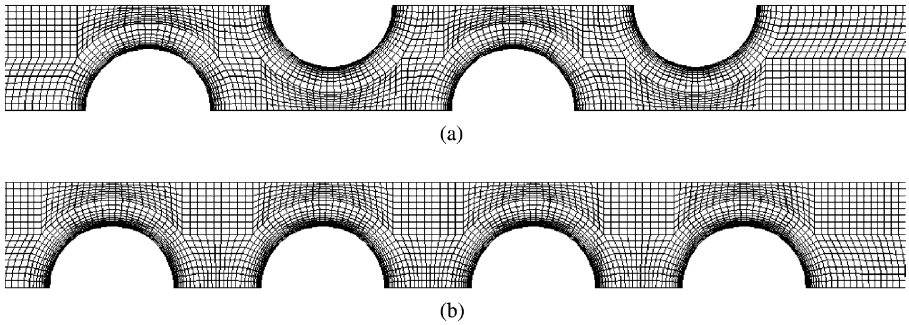

Fig. 3. Grid generations for (a) staggered and (b) in-line arrangements.

Table 1
Dimensions of bundles used in numerical investigation

	Staggered					In-line		
	s1	s2	s3	s4	s5	i1	i2	i3
Tube outside diameter, d	24	24	24	24	24	24	24	24
Fin diameter, d_f	34	34	34	44	44	34	34	34
Fin height, h_f	5	5	5	10	10	5	5	5
Fin thickness, t_f	0.5	0.5	0.5	0.5	0.5	0.5	0.5	0.5
Fin spacing, s	1.6	2	4	0.7	2	1.6	2	4
Fin pitch, $S_f = s + t_f$	2.1	2.5	4.5	1.2	1.2	2.1	2.5	4.5
Transverse tube pitch, S_t	40.8	40.8	40.8	52.8	52.8	40.8	40.8	40.8
Longitudinal tube pitch, S_l	35.33	35.33	35.33	45.73	45.73	40.8	40.8	40.8
Number of rows, n	4	4	4	4	4	4	4	4

All dimensions are in mm.

Using this air-side heat flow rate, the heat transfer coefficient h can be evaluated by means of Eq. (10) where A_t is the tube surface area except fin, A_f is the fin surface area and η is the fin efficiency.

$$h = \frac{\dot{Q}}{(A_t + \eta A_f)\theta} \tag{10}$$

Therein the heat transfer coefficients at the fin and base tube surfaces are assumed to be the same. θ is the log mean temperature difference,

$$\theta = \frac{T_{in} - T_{out}}{\ln \frac{T_{in} - T_w}{T_{out} - T_w}} \tag{11}$$

The fin efficiency, which is needed to determine the heat transfer coefficient, arises from iterative calculations of Eqs. (12) and (13) and the heat transfer coefficient from Eq. (10). The value of ψ was derived from Eq. (14) individually [23].

$$\eta = \frac{\tanh(\psi m h_f)}{\psi m h_f} \tag{12}$$

$$m = \sqrt{\frac{2h}{k_f t_f}} \tag{13}$$

$$\psi = 1.0 + 0.35 \ln\left(1.0 + 2.0\frac{h_f}{d}\right) \tag{14}$$

The heat transfer coefficient and pressure drop are expressed in the dimensionless form by the Nusselt and Euler numbers

$$Nu = \frac{hd}{k_a} \tag{15}$$

$$Eu = \frac{\Delta p}{\rho u_{max}^2} \tag{16}$$

$$Eu_m = \frac{\Delta p}{\rho u_m^2} \tag{17}$$

4. Results and discussion

4.1. Global flow behaviour

The global velocity distribution in the bundle is essential for understanding of the local flow and heat transfer phenomena. Fig. 4 shows for both the staggered and the in-line arrangement velocity fields in a cross-section mid-plane between two adjacent fins. It is clearly shown that the flow pattern around the first rows of both of the arrangements is very similar. The air flow is strongly accelerated in the passages between two tubes with maximum velocities lateral to the deeper rows of the staggered bundle due to respective deflections. For this arrangement, the main stream is imposed upon higher percentage of the fin surface than in the in-line array where much larger wake regions establish with stagnant or even reverse flow.

4.2. Local flow behaviour

The velocity and temperature boundary layers on the fin and tube surfaces strongly depend on the spacing between the fins and the corresponding velocity. Numerical results will be presented in Figs. 5–7 which are obtained for three different fin spacings (1.6, 2 and 4 mm) at fixed fin height (5 mm), tube diameter (24 mm) and both staggered and in-line arrangements. The figures show respective velocity and temperature distributions in cross-sections upstream of the stagnation points ($\beta = 0°$) of each tube.

Fig. 5 shows velocity distributions between the fins of the first rows at $Re = 8.6 \times 10^3$. Analysis of these velocity fields yields almost identical flow patterns for both of the arrangements and, therefore, only the staggered results have been plotted. For the narrowest fin spacing (1.6 mm), two boundary layers grow from the leading edge of the fins to a maximum thickness close to the junction of fin base and tube surface. Owing to the adverse pressure gradient effect, horseshoe vortices

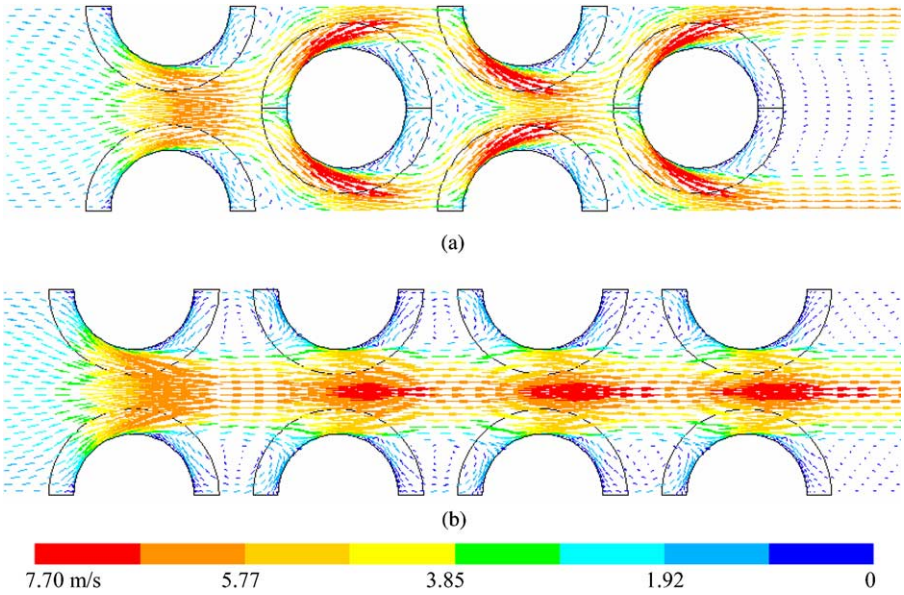

Fig. 4. Global velocity distributions for (a) staggered and (b) in-line arrangements at $Re = 8.6 \times 10^3$.

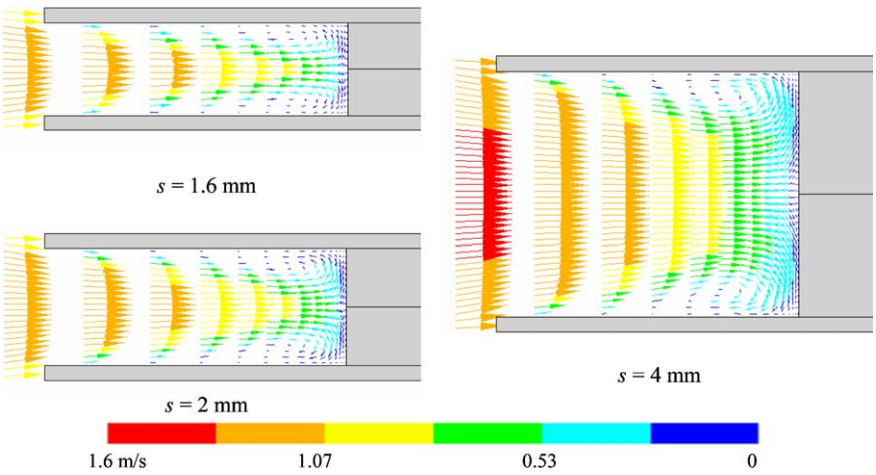

Fig. 5. Velocity distributions between fins of first rows in staggered arrangement at $Re = 8.6 \times 10^3$.

develop near the junction, which are found to be more obvious for the larger spacings (2 and 4 mm). When increasing the Reynolds number to $Re = 4.3 \times 10^4$, the flow fields for the first rows are found to be very similar to the low *Re* case, as plotted in Fig. 6a (the two pictures on the left hand side) for $s = 4$ mm as an example with increased velocity and, by this, reduced thickness of the boundary layer. However, in the present simulations it is not possible to observe further vortices as described by Sung et al. [1] since these are very small. An appropriate numerical simulation may require an extremely refined grid.

It is a well-known phenomenon that the deeper rows in a bundle are affected by the upstream ones as shown in Fig. 4. This is especially true for the in-line arrangement where the second and subsequent rows are in the wake region of the preceding ones. In the staggered array the first row acts as a turbulence promoter as well as the velocity is increased for the further rows because of its blockage effect [10]. Fig. 6a (right hand side) shows flow patterns between the fins of the fourth row for both of the arrangements. For the staggered case (the upper one) it is almost inevitable that the velocity boundary layer at the fin base and tube surface becomes thinner

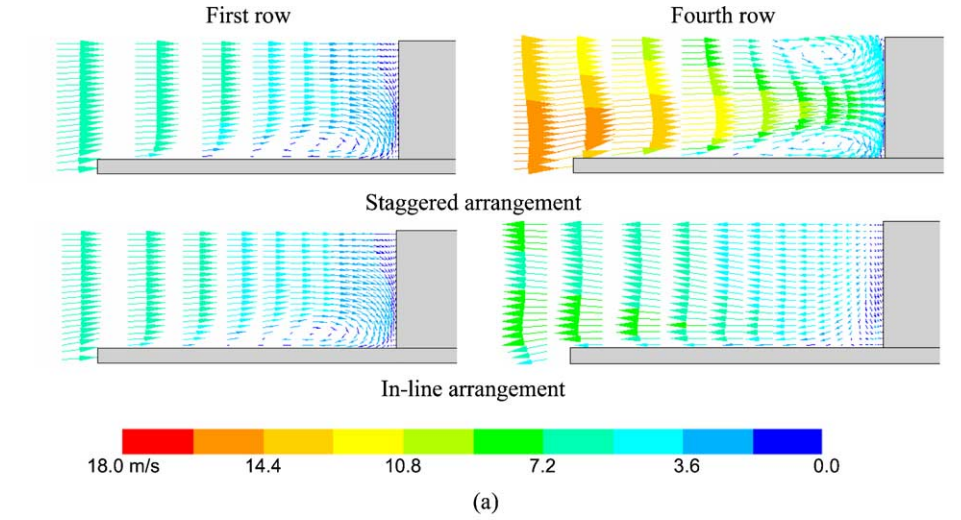

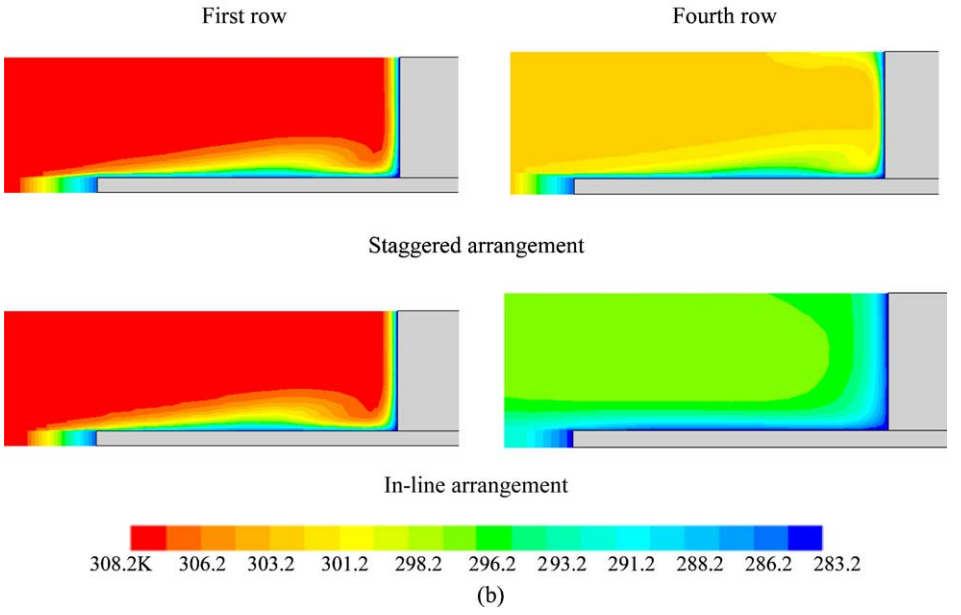

Fig. 6. (a) Velocity and (b) temperature distributions between the fins of $s = 4$ mm at $Re = 4.3 \times 10^4$.

due to the apparently more prominent horseshoe vortex system when compared with the first row.

Surprisingly, in Fig. 6a a secondary vortex system occurs in the fourth row (and also in the third one, not shown here) of the $s = 4$ mm staggered bundle. The size of the second vortex is almost the same as the first one close to the fin-tube junction. Although it is difficult to find the responsible flow features, here are three possible reasons for the presence of these vortices: the higher Re number, the larger fin spacing and the wake effect of the preceding rows could cause such vortices. Unfortunately, no experimental flow visualization data are available for verification.

Observation of the in-line arrangement (the lower case in Fig. 6a), however, shows a completely different behaviour. Reverse flow is found upstream of the fourth row instead of the horseshoe vortex system due to the wake-position of all the tubes downstream the first one (see Fig. 4). It has to be noted that the in-line array exhibits smaller averaged heat transfer coefficients than the staggered one since large parts of the fin surface in the surroundings of the upper and lower stagnation point of all tubes lie within the wake flows except for the first row. In considering the fourth row results, it is appropriate to mention that there may develop a horseshoe vortex system if the longitudinal pitch is long enough.

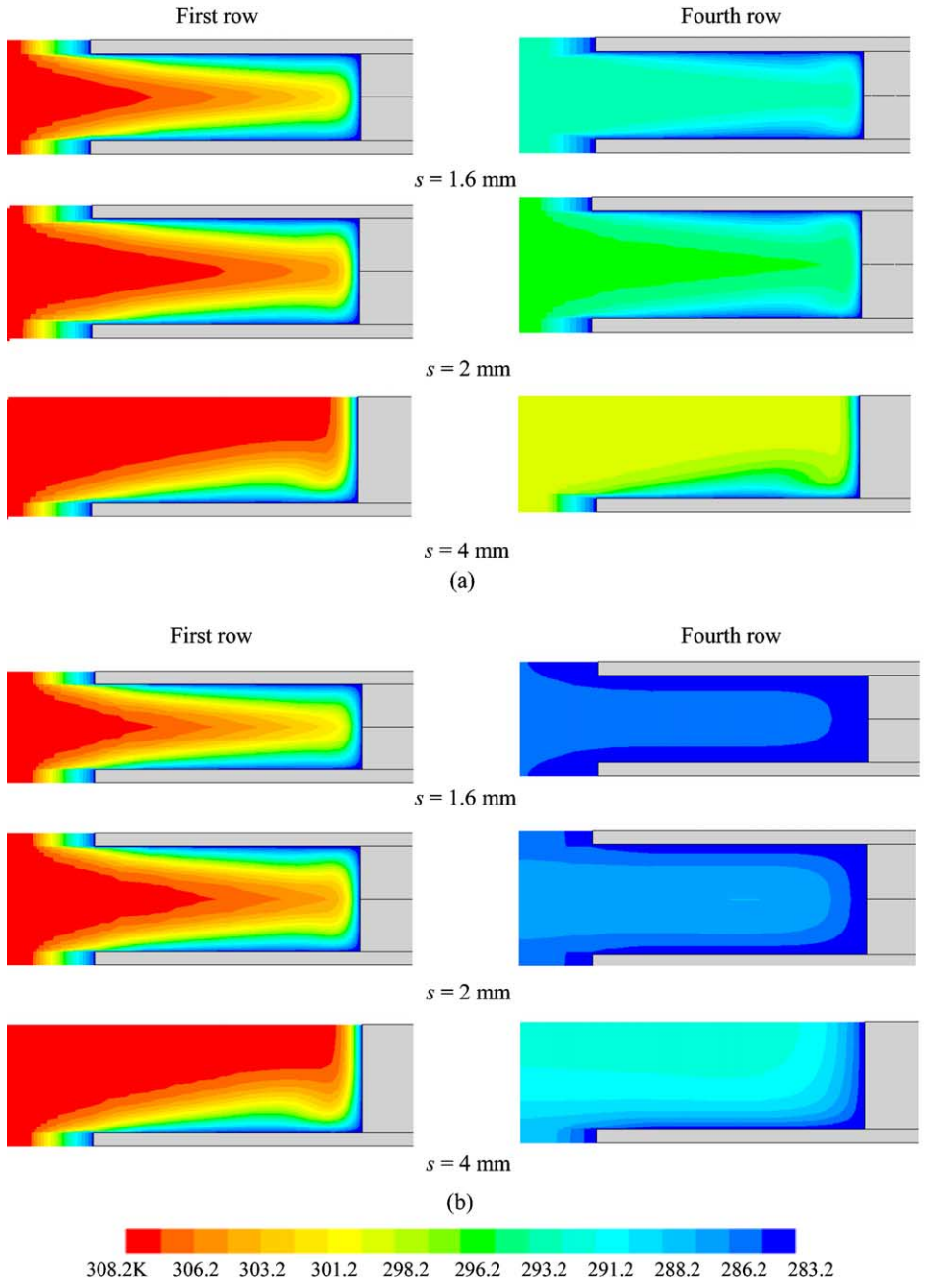

Fig. 7. Temperature distributions between the fins for (a) staggered and (b) in-line arrangements at $Re = 8.6 \times 10^3$.

4.3. Thermal boundary layer development

The presence of the horseshoe vortices evidently causes effects on the thermal boundary layer formation since the temperature gradient at the surface depends on the flow field. The results obtained for the three different spacings will be utilized for the analysis of the thermal boundary layer development. This is shown in Fig. 6b for the $s = 4$ mm case at $Re = 4.3 \times 10^4$ in both of the arrangements. As the velocity profiles of the first rows are similar for both arrays, nearly identical temperatures distributions are also obtained. However, the situation changes when going deeper into the bundles. It is seen from the staggered fourth row figure that the temperature gradient at the symmetry line (at the upper end of the plot) is slightly reduced owing to the secondary

horseshoe vortex (in the staggered case) and to the reverse flow (for the in-line array) as seen in Fig. 6a.

Now the attention will be focused on the thermal boundary layer development at $Re = 8.6 \times 10^3$ and the results shown in Fig. 7 for the three different spacings. Examination of the first rows of staggered (Fig. 7a) and in-line arrays (Fig. 7b) shows that at the narrowest fin spacing bundle, the two boundary layers grow to touch each other, independently from the kind of arrangement which again has no effect on the first-row behaviour. Thus, the main flow cannot sufficiently penetrate to reach the tube's surface. The temperature gradient at the fin base and the tube surface is very small as shown in the figure, which will lead to a decrease of the convection heat transfer coefficient. For moderately spaced fins ($s = 2$ mm) the thermal boundary layers are slightly thinner than in the first case and it is observed that the boundary layer interacting point is shifted markedly. As a result, the heat transfer coefficient will increase. In the third case with $s = 4$ mm, the boundary layers are found to develop independently from each other. According to the horseshoe vortex close to the fin-tube junction the temperature gradient is much higher there than for the lower-spacing cases. Therefore, the boundary layer development at both the fin and the tube surface are mainly dependent on the fin spacing.

Considering the fourth-row positions of staggered array (Fig. 7a, right hand side) the temperature boundary layers are found to be thinner than those of the first rows. It is clearly seen from the fourth row figures that the boundary layers develop separately even for the narrowest fin spacing. Further inspection of the figures shows that the temperature between the fins is decreased significantly compared to the first row results. Naturally, the main air stream becomes cooler for subsequent rows.

Now attention will be turned to the in-line arrangement (Fig. 7b). Because of the in-line tubes position, the temperature difference between air and fins is considerably lower than for the staggered arrangement. The in-line fourth row has a lower temperature gradient than the first row. For the case of the lowest fin spacing, the air temperature near the tube surface is almost the same as surface temperature. The temperature gradient increases with fin spacing due to the enhanced flow velocity.

4.4. Fin spacing effects on heat transfer and pressure drop characteristics

The heat transfer and pressure drop results are plotted in Fig. 8 versus the fin spacing to height ratio s/h_f with *Re* number and kind of arrangement as the parameters. In case of the staggered array the heat transfers coefficient are found to increase up to $s/h_f = 0.32$ and then, they keep almost constant for the further increments with

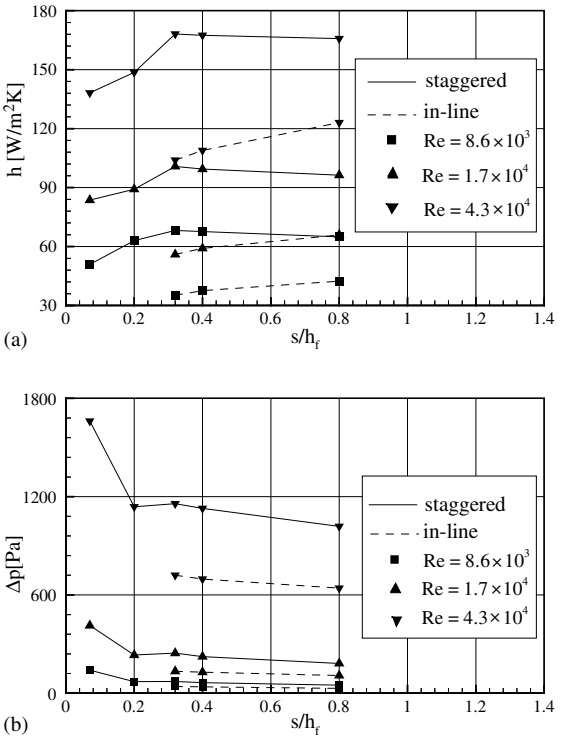

Fig. 8. Effects of fin spacing to height ratio on (a) heat transfer coefficient and (b) pressure drop for staggered and in-line bundles.

some tendency to decrease (by about 1.4%). Antufév and Gusev [7] also found that the heat transfer coefficients decrease in the range of $s/h_f = 0.4$ to 0.57 where the tube diameter has been 19 mm.

Experimental results reported in [2,3,6] yield negligible spacing effects on heat transfer when s exceeds about twice the boundary layer thickness at the base of fin. These results are well consistent with the present numerical staggered array investigations in which most of the boundary layers between the fins are found to depart from each other. Therefore, it is confirmed that the effect of fin spacing is largely influenced by the boundary layer development in the system.

The numerical simulation for the in-line tube array shows a different trend: the heat transfer coefficient of the bundle increases with s/h_f in all the considered cases. This trend may be attributed to the in-line array geometry where the deeper rows lie in the wake region of the previous tubes. Due to the wider fin spacing, an increased mass flow can penetrate the in-line tubes surfaces and a stronger reverse flow appears in the wake. Both of the flow effects enhance heat transfer. When increasing the s/h_f from 0.32 to 0.8, the increment of the heat transfer coefficient is about 19%.

Similar to the experimental results of Jameson [5], Fig. 8b shows that the pressure drop decreases for both

of the tube arrays while increasing the s/h_f where the strong interactions of boundary layers between the fins are reduced, and the same holds for the friction losses. As expected, the staggered tube array gives a larger pressure drop especially at the higher *Re* numbers.

4.5. Data comparison

The present numerical heat transfer and pressure drop results will now be compared with the predictions of experimental-based correlations from the literature. *Nu* numbers obtained by the numerical simulations of the staggered arrangements (see Table 1) have been modified according to the correlations of Briggs and Young [4], Schmidt [23] and VDI-Wärmeatlas [24], and the results are plotted vs. Reynolds numbers in Fig. 9. The numerical results are found to be in good agreement with those of the VDI-Wärmeatlas [24] and all points are within ±15%, as can be seen in Fig. 9c. From Fig. 9a and b, for correlations obtained by Briggs and Young [4] and Schmidt [23] most of the points spread in the range ±25%.

The heat transfer results for in-line arrangement are illustrated in Fig. 10. It is seen from Fig. 10b that the numerical results agree well with the correlation of VDI-Wärmeatlas [24] and the maximum difference between the individual points does not exceed ±15% while Schmidt's correlation is deviated up to −20% (Fig. 10a).

In Fig. 11, the pressure drop results are compared with the correlations of Robinson and Briggs [22], and Haaf [25] in terms of Euler number. It is observed from Fig. 11a that the numerical results deviate by more than ±40% from the Robinson and Briggs's correlation where parameters for the finning geometry variables such as fin spacing, fin height and fin thickness are absent. In Fig. 11b, Reynolds number is based on the equivalent diameter and average velocity in the bundle as given in the nomenclature and Euler number is based on the average velocity. It is seen that most of the numerical

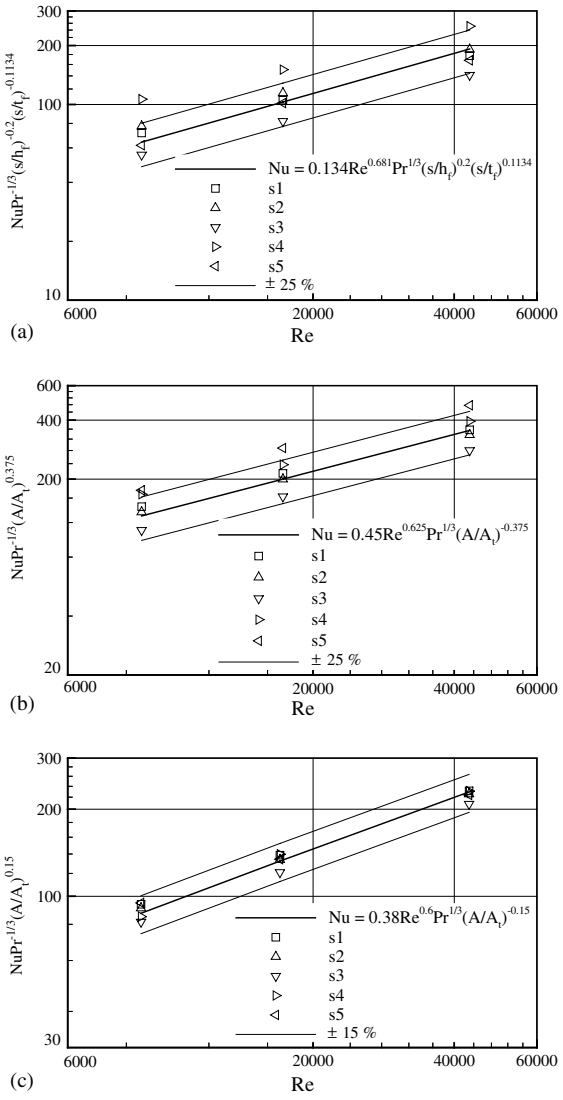

Fig. 9. Comparisons of heat transfer results with (a) Briggs and Young [4], (b) Schmidt [23] and (c) VDI [24] correlations for staggered arrangement.

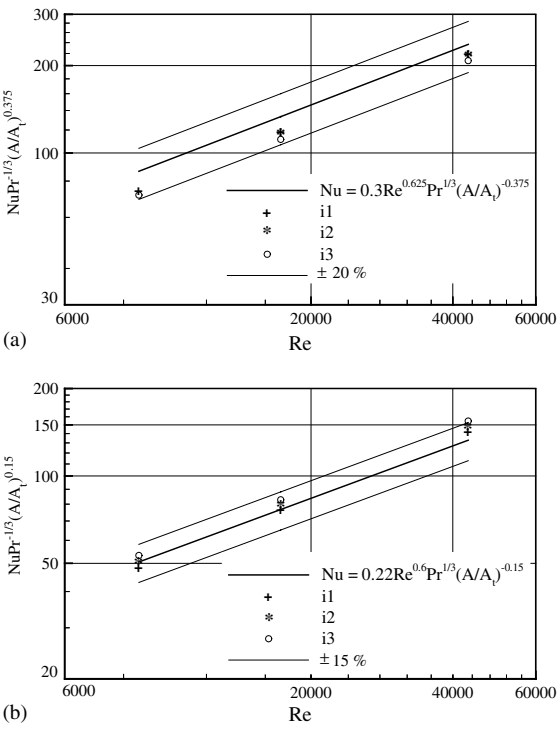

Fig. 10. Comparisons of heat transfer results with (a) Schmidt [23] and (b) VDI [24] correlations for in-line arrangement.

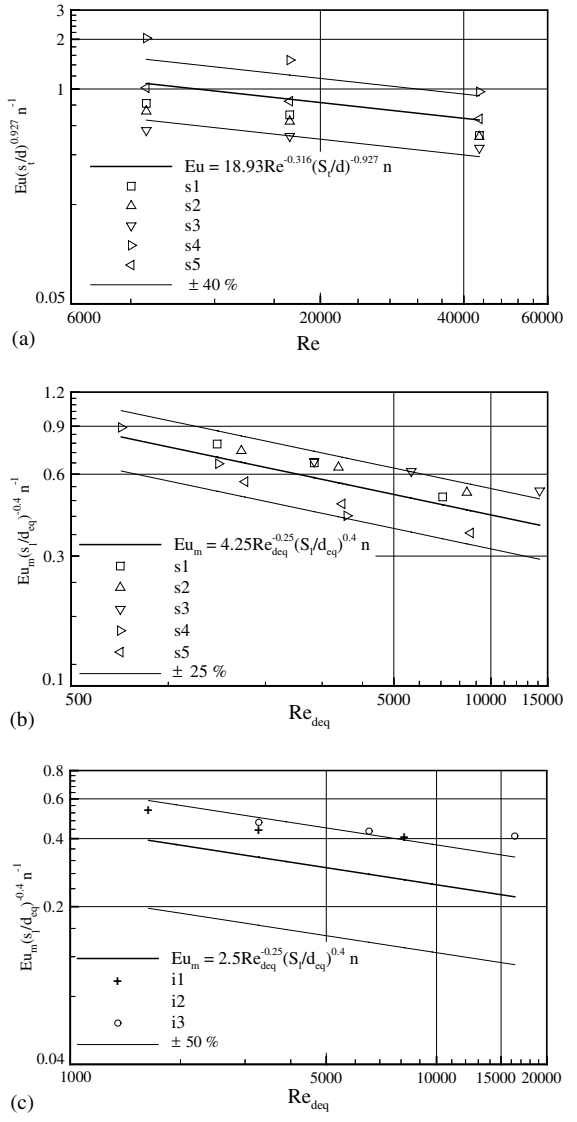

Fig. 11. Comparisons of pressure drop results with (a) Robinson and Briggs [22], (b) Haaf [25] correlations for staggered, and (c) Haaf [25] correlation for in-line arrangement.

results are spread within ±25% of Haaf's correlation. Numerical results for the in-line arrangement are depicted in Fig. 11c and the present results are found to exceed those of the Haaf's correlation by more than 50%.

5. Conclusions

Heat transfer and pressure drop characteristics on the air-side of annular-finned tube heat exchangers have been determined numerically. The flow visualization results reveal important aspects of the local heat transfer and flow features of the annular-finned tube bundles. The horseshoe vortex effect is more obvious in the largest fin spacing and at the high velocity. The boundary layer development on the fin and tube surfaces mainly depends on the fin spacing to height ratio s/h_f. For the range of study, the heat transfer coefficient of the staggered arrangements is found to increase with s/h_f up to $s/h_f = 0.32$ and then, it keeps almost constant. For in-line arrangement, the heat transfer coefficient increases in the whole investigated parameter range. The pressure drop decreases for both tube arrays when s/h_f is increased. Heat transfer results agree well with existing experimental correlations. For the pressure drop, numerical results deviate much more from available correlations, especially for in-line cases.

Acknowledgements

The support of this work by the Deutscher Akademischer Austauschdienst (DAAD) is greatly appreciated.

References

[1] H.J. Sung, J.S. Yang, T.S. Park, Local convective mass transfer on annular cylinder with transverse annular fins in cross flow, Int. J. Heat Mass Transfer 39 (1996) 1093–1101.
[2] V.B. Kuntysh, I.G. Taryan, F.M. Yokhvedov, On the effect of the relative depth of the interfin space on heat transfer from bundles of finned tubes, Heat Transfer—Sov. Res. 6 (6) (1974) 5–9.
[3] J. Stasiulevičius, A. Skrinska, Heat Transfer of Finned Tube Bundles in Crossflow, Hemisphere Publishing, 1988.
[4] D.E. Briggs, E.H. Young, Convection heat transfer and pressure drop of air flowing across triangular pitch banks of finned tubes, Chem. Eng. Progr. Symp. Ser. 59 (41) (1963) 1–10.
[5] S.L. Jameson, Tube spacing in finned tube banks, ASME Trans. 67 (1945) 633–642.
[6] B. Watel, S. Harmand, B. Desmet, Influence of flow velocity and fin spacing on the forced convective heat transfer from an annular-finned tube, JSME Int. J., Ser. B 42 (1) (1999) 56–64.
[7] V.M. Antuf'ev, E.K. Gusev, Intensification of heat transfer of cross-flow finned surfaces, Teploenergetika 15 (7) (1968) 31–34.
[8] X. Hu, A.M. Jacobi, Local heat transfer behaviour and its impact on a single-row annularly finned tube heat exchanger, ASME J. Heat transfer 115 (1993) 66–74.
[9] F.E.M. Saboya, E.M. Sparrow, Local and average transfer coefficients for one-row plate fin and tube heat exchanger configuration, ASME J. Heat Transfer, Ser. C 96 (3) (1974) 265–272.
[10] F.E.M. Saboya, E.M. Sparrow, Transfer characteristics of two-row plate fin and tube heat exchanger configurations, Int. J. Heat Mass Transfer 19 (1976) 41–49.

[11] T.W.H. Sheu, S.F. Tsai, A comparison study on fin surface in finned-tube heat exchangers, Int. J. Numer. Meth. Heat Fluid flow 9 (1) (1999) 92–106.
[12] A.M. Jacobi, R.K. Shah, Air-side flow and heat transfer in compact heat exchangers: a discussion of enhancement mechanisms, Heat Transfer Eng. 19 (4) (1998) 29–41.
[13] G.N. Xi, K. Torikoshi, Computation and visualization of flow and heat transfer in finned tube heat exchangers, International Symposium on Heat Transfer, Tsinhua University, Beijing China (7.10–11.10), 1996, pp. 632–637.
[14] M. Fiebig, A. Gorsse-Georgemann, Y. Chen, N.K. Mitra, Conjugate heat transfer of a finned tube part A: Heat transfer behaviour and occurrence of heat transfer reversal, Numer. Heat Transfer, Part A 28 (1995) 133–146.
[15] K. Torikoshi, G. Xi, Y. Nakazawa, H. Asano, Flow and heat transfer performance of a plate-fin and tube heat exchanger, first report: effect of fin pitch, in: Proceeding of the Tenth International Heat Transfer Conference, 1994, pp. 411–416.
[16] S. Kaminski, Numerische Simulation der luftseitigen Strömungs-und Wärmetransportvorgänge in Lamellenrohr-Wärmeübertragen, Doctoral Thesis, Freiberger Forschungshefte, A 867 Energie, 2002.
[17] S. Kaminski, U. Gross, Luftseitige Transportprozesse in Lamellenrohrbundeln numerische Untersuchung, Kl Luft- und Kältetechnik 39 (2003) 220–224.
[18] R. Romero-Méndez, M. Sen, K.T. Yang, R. McClain, Effect of fin spacing on convection in a plate fin and tube heat exchanger, Int. J. Heat Mass Transfer 43 (2000) 39–51.
[19] J.Y. Jang, J.T. Lei, L.C. Liu, The thermal-hydraulic characteristics of staggered annular finned-tube heat exchangers under dry and dehumidifying conditions, Int. J. Heat Mass Transfer 41 (1998) 3321–3337.
[20] M.S. Mon, Numerical investigation of air-side heat transfer and pressure drop in circular finned-tube heat exchangers, Doctoral Thesis, Technische Universität Bergakademie Freiberg, Germany, 2003.
[21] R.L. Webb, Air-side heat transfer in finned tube heat exchanger, Heat Transfer Eng. 1 (3) (1980) 33–49.
[22] K.K. Robinson, D.E. Briggs, Pressure drop of air flowing across triangular pitch banks of finned tubes, Chem. Eng. Progr. Symp. Ser. 62 (64) (1966) 177–184.
[23] Th.E. Schmidt, Der Wärmeübergang an Rippenrohre und die Berechnung von Rohrbündel-Wärmeaustauschern, Kältetechnik, Band 15, Heft 12, 1963.
[24] Verein Deutscher Ingenieure, VDI-Wärmeatlas., Berechnungsblätter für den Wärmeübergang, 8. Aufl. Berlin u.a., Springer, 2000.
[25] S. Haaf, Wärmeübertragung in Luftkühlern, Handbuch der Kältechnik, Bd. 6, Teil B: Wärmeaustauscher, Berlin u.a.: Springer Verlag, 1988, pp. 435–491.
[26] FLUENT Incorporated, FLUENT 5 User's Guide, Fluent Incorporated Lebanon, NH-USA, 1998.